Earth and Planetary Science Letters 592 (2022) 117595

Contents lists available at ScienceDirect

Earth and Planetary Science Letters

www.elsevier.com/locate/epsl

Geologically constrained astronomical solutions for the Cenozoic era

Richard E. Zeebe [a,*], Lucas J. Lourens [b]

[a] School of Ocean and Earth Science and Technology, University of Hawaii at Manoa, 1000 Pope Road, MSB 629, Honolulu, HI 96822, USA
[b] Department of Earth Sciences, Faculty of Geosciences, Utrecht University, Princetonlaan 8a, 3584 CB Utrecht, Netherlands

ARTICLE INFO

Article history:
Received 22 January 2022
Received in revised form 3 May 2022
Accepted 6 May 2022
Available online xxxx
Editor: Y. Asmerom

Dataset link: http://www2.hawaii.edu/~zeebe/Astro.html

Dataset link: https://www.ncei.noaa.gov/access/paleo-search/study/36415

Keywords:
astronomical timescale
astronomical solutions
solar system chaos
geological timescale
Paleocene
end Cretaceous

ABSTRACT

Astronomical solutions provide insight into the Solar System's dynamical evolution and are indispensable tools in cyclostratigraphy and astrochronology. Constructing an absolute, fully calibrated astronomical time scale (ATS) has hitherto been hindered beyond ~50 Ma because orbital calculations disagree before that age due to solar system chaos. We have recently developed a new approach that allows extending the fully calibrated astronomical time scale to ~58 Ma. Here, we present geologic data and new astronomical solutions, extending our approach across the Paleocene epoch (~66 to ~56 Ma). New astronomical solutions were generated using numerical solar system integrations following our earlier work, which now provides geologically constrained astronomical solutions for the Cenozoic era (66-0 Ma). The orbital solutions are available to 300 Ma — we caution, however, that the time interval 300-66 Ma is unconstrained due to dynamical chaos in the solar system. We have tested the sensitivity of our new solutions to various parameters, including numerical stepsize, solar quadrupole moment, number of asteroids included, initial positions, and tidal dissipation. We demonstrate that our new solutions yield improved agreement with the geologic record across the Paleocene epoch, compared to previously available astronomical solutions for that period. Furthermore, we discuss implications of our results for solar system chaos and resonance transitions. We have also obtained K/T boundary (KTB) ages based on our new solutions, which suggest slightly younger KTB ages than those inferred from most recent $^{40}Ar/^{39}Ar$ radiometric dating.

1. Introduction

"To place all the scattered pages of earth history in their proper chronological order is by no means an easy task" (Arthur Holmes, father of the geologic time scale, see Holmes (1965); Gradstein et al. (2012)). Nonetheless, significant progress has been made over the past few decades in ordering these scattered pages through deep-sea drilling and astronomical calculations for Earth's orbital parameters to calibrate critical intervals of the geologic time scale, particularly in the early and mid-Cenozoic (e.g., Hilgen et al., 2015; Hinnov, 2000; Laskar et al., 2011a; Lauretano et al., 2018; Liebrand et al., 2016; Li et al., 2018; Lourens et al., 2005; Meyers, 2015; Westerhold et al., 2008; Zeebe, 2017; Zeebe and Lourens, 2019).

Development of an astronomical time scale (ATS) based on astronomical solutions (calculated planetary orbital parameters) has transformed the dating of geologic archives and today represents the backbone of cyclostratigraphy and astrochronology, widely used in geology, geophysics, paleoclimatology, and more. Importantly, the utility of absolute geologic ages and chronologies reaches far beyond mere archiving and cataloging of Earth's history. For example, accurate absolute ages of past climate-carbon cycle events relative to the timing of forcings such as volcanism, impacts, orbital forcing, etc. are critical to understand drivers and triggers of environmental changes and catastrophes (e.g., Cramwinckel et al., 2018; Gradstein et al., 2012; Lantink et al., 2019). Moreover, the relative timing of events (detailed chronology) is essential to understanding both past changes in long-term climate and rapid climate events. The chronology of the early Eocene hyperthermals (extreme global warming events) in relation to orbital forcing represents just one example (e.g., Lauretano et al., 2016, 2018; Lourens et al., 2005; Zeebe and Lourens, 2019). Hyperthermals are considered the best paleo-analogs for massive carbon release and the climate response to anthropogenic carbon release (e.g., Zachos et al., 2005; Zeebe et al., 2016). However, understanding and projecting future climate change (informed by paleoclimate studies) requires accurate dating of past forcing events to identify similarities and differences to present and future forcings.

We have recently provided a fully calibrated ATS to ~58 Ma and a revised age for the Paleocene-Eocene boundary with a small

* Corresponding author.
E-mail addresses: zeebe@soest.hawaii.edu (R.E. Zeebe), L.J.Lourens@uu.nl (L.J. Lourens).

https://doi.org/10.1016/j.epsl.2022.117595
0012-821X/

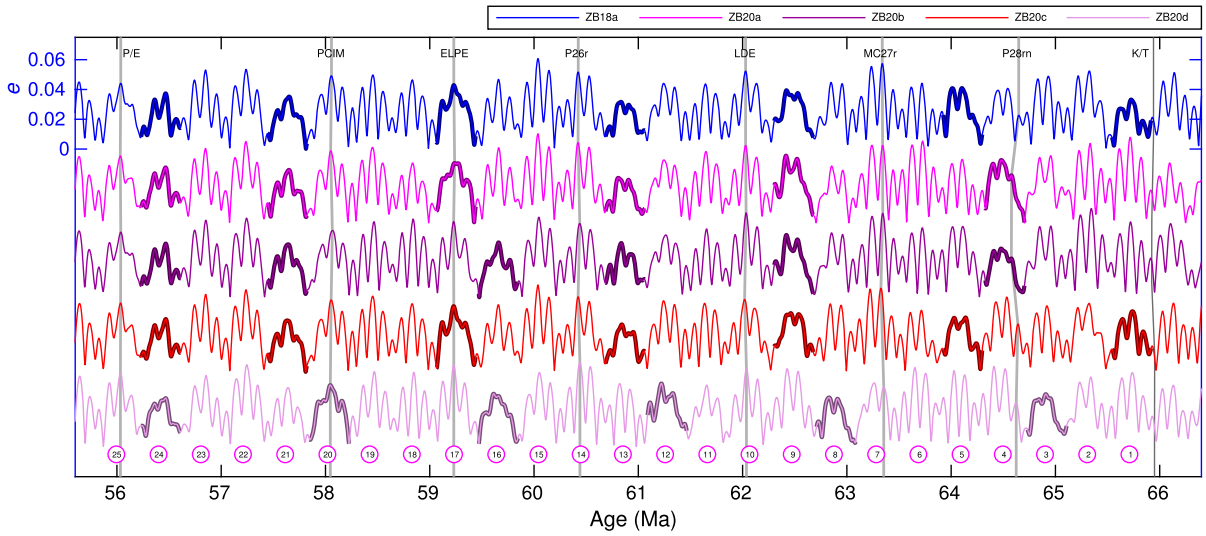

Fig. 1. New astronomical solutions ZB20a, ZB20b, ZB20c, and ZB20d (this study) and ZB18a (Zeebe and Lourens, 2019) across the Paleocene (Earth's orbital eccentricity vs. age). Solutions ZB20*x* are plotted with an arbitrary negative offset. P/E = Paleocene/Eocene boundary, PCIM = Paleocene Carbon Isotope Maximum, ELPE = Early Late Paleocene Event, P26r = Peak Chron 26r (middle), LDE = Latest Danian Event, MC27r = Middle Chron 27r event, P28rn = Peak near C28r/C28n boundary (Site 1209), K/T = K/T boundary (informal use, see ICS, 2005). Circled numbers 1–25 indicate long eccentricity (405 kyr) cycles counted from the K/T boundary upwards. Solution cycles highlighted in bold correspond to very long eccentricity nodes (VLNs) with reduced ∼100-kyr amplitude. (For interpretation of the colors in the figure(s), the reader is referred to the web version of this article.)

margin of error (Zeebe and Lourens, 2019). However, an equivalent, detailed chronology for events across the full Paleocene based on specific astronomical solutions is still missing. As a result, Paleocene records have been interpreted differently regarding the number of 405-kyr cycles contained therein (Hilgen et al., 2010, 2015; Westerhold et al., 2008); although progress has been made for the early Paleocene (e.g., Dinarès-Turell et al., 2014; Hilgen et al., 2015). Because of uncertainties in radiometric dating calibrations, the disagreement has led to different proposed ages for the K/T boundary (T = Tertiary is used informally here, not as a formal division, see ICS (2005)). Furthermore, due to the lack of a specific astronomical solution (constrained by Paleocene data records), the solar system's chaotic evolution is hitherto unknown for this interval. Fundamental to resolving the challenges above is development of an absolute, fully calibrated ATS beyond ∼58 Ma based on specific astronomical solutions, which has hitherto been hampered because orbital calculations disagree before ∼50 Ma due to solar system chaos. Here we provide new astronomical solutions and a fully calibrated ATS including the Paleocene (∼66-56 Ma), which, combined with our recent work (∼58-0 Ma, Zeebe and Lourens (2019)), spans the entire Cenozoic.

In the following, we first introduce our new astronomical solutions (Section 2, numerical methods are summarized in Appendix A). Next, we present a simplified, initial approach to calibrating the Paleocene ATS (Section 3), followed by a detailed age model based on cyclostratigraphy from Ocean Drilling Program (ODP) Sites 1262/1209, and Zumaia, Spain (Section 4). Additional information about the detailed age model (which is based on eccentricity), depth/age windows, etc. can be found in Appendix B; the lack of suitable Paleocene obliquity records is discussed in Appendix C. Our K/T boundary ages based on the new astronomical solutions are presented in Section 5. Finally, we discuss solar system chaos and resonance transitions in relation to our astronomical solutions in Section 6. Below, the terms short eccentricity (e_s) and long eccentricity (e_l) cycle refer to cycles related to the 100- and 405-kyr periodicity in Earth's orbital eccentricity, respectively. The term very long eccentricity node (VLN) refers to intervals of reduced ∼100-kyr amplitude (highlighted in Fig. 1).

2. New astronomical solutions

New astronomical solutions were generated using solar system integrations following our earlier work (Zeebe, 2015a,b, 2017; Zeebe and Lourens, 2019, 2022); for numerical methods, see Appendix A. The primary objective of the simulations was to find solutions for the Paleocene that are very close to the solution ZB18a from ∼58 Ma to 0 Ma but differ from ZB18a for ages prior to ∼58 Ma. ZB18a shows exceptional agreement with geologic data from ∼58 to 53 Ma (Zeebe and Lourens, 2019). Our approach hence provides a variety of solutions (in addition to ZB18a) for testing against the geologic record before ∼58 Ma. We used the difference in Earth's orbital eccentricity (Δe) to track the difference between two solutions, considered to diverge at time τ when $\max|\Delta e|$ irreversibly crosses ∼10% of mean e ($\sim 0.028 \times 0.1$), going backwards in time (see Zeebe, 2017). For most integrations, the same initial conditions for positions and velocities were used as for ZB18a (JPL ephemeris DE431, see Appendix A). We also tested the latest JPL ephemeris DE441 (Park et al., 2021), which has a small effect on the results, i.e., the divergence time relative to ZB18a (based on DE431) is $\tau \simeq 66$ Ma. For consistency with ZB18a, we used DE431 for our new solutions (ZB20*x*) presented below. In one set of simulations ($N = 40$), we used initial conditions from the ephemeris INPOP08a for which τ's turned out to be $\gtrsim$54 Ma. Note that solutions based on INPOP08a (Laskar et al., 2011a) fit the geologic record better than those based on more recent INPOP versions, despite INPOP08a being considered less accurate (see also Appendix A.1 and Supplement of Zeebe and Lourens, 2019).

To obtain a variety of solutions, we varied several parameters within reasonable uncertainty bounds (if applicable), including the integration timestep Δt, the solar quadrupole moment J_2 (for a discussion of J_2 values, see Section A.1), the number of asteroids $N_{\rm ast}$ included in the simulation, Earth's initial position (radial distance Δr_0), and the tidal dissipation in the Earth-Moon system T_d (see Table 1). In total, more than 1,700 solar system integrations over the past 100 Myr were performed for the current project. Note that we provide most of our solutions over the time interval from 100-0 Ma (ZB18a and ZB20*x* over 300-0 Ma). However, as we only provide an analysis for the Paleocene/Cenozoic here, we caution that the interval prior to 66 Ma is unconstrained due to

Table 1
Parameter variations for astronomical solutions.

Parameter	Symbol	Unit	Std. ZB18a	Range	τ[a] (Ma)
Timestep[b]	Δt	days	2.0	2.0–3.21875	$\gtrsim$70
Solar quadrupole moment[c]	J_2	$\times 10^7$	1.305	1.15–1.64	$\gtrsim$53
Number of asteroids	N_{ast}	–	10	10–50	$\gtrsim$55
Δ Initial position[d]	Δr_0	m	0	~0–900	$\gtrsim$66
Tidal dissipation[e]	T_d	–	0	0–1	$\gtrsim$60

[a] Divergence time relative to run with standard (Std.) values for all other parameters (i.e., values for ZB18a).
[b] In increments of 2^{-5} d = 0.03125 d.
[c] For discussion of J_2 values, see Section A.1.
[d] Radial distance.
[e] Fraction of modern value (see text).

solar system chaos. The divergence times (τ's) for our variations in Δt and Δr_0 are older than ~66 Ma (see Table 1). That is, from ~66-0 Ma the solutions are very close to ZB18a and hence provide no new information for the astronomical calibration of geologic time across the Paleocene. Extending the maximum Δr_0 for Earth beyond the values tested here appeared unrealistic as ~900 m already exceeds the uncertainty limits for the orbits of the terrestrial planets of a few hundred meters (Fienga et al., 2014; Folkner et al., 2014; Viswanathan et al., 2017).

We also ran a large number of simulations in which we varied Δr_0 for Earth and Jupiter simultaneously. While some of those solutions showed good agreement with the geologic data, i.e., small RMSDs (root mean square deviations) across certain depth/age windows (see Appendix B), their short eccentricity (e_s) cycle amplitude at events such as P28rn was unacceptably weak (see Fig. 1, Appendix B). Variations in the tidal dissipation parameter of the Earth-Moon system (T_d) led to discernible differences for $\tau \gtrsim 60$ Ma. Tidal dissipation causes slow changes in the lunar orbit and hence in the gravitational interaction with (and ultimately the orbits of) other solar system bodies, including the orbit of the Earth (or the Earth-Moon barycenter). This applies to solar system integrations in which the Moon is included as a separate object or the Earth-Moon system is modeled as a gravitational quadrupole. The parameter T_d used here is nondimensional and measures the tidal dissipation relative to the modern value at $t = 0$, i.e., $T_d = Q_t/Q_0$, where $Q_0 = (dn_L/dt)_0/n_{L0} = -4.6 \times 10^{-18}$ s^{-1} and n_L is the lunar mean motion (Quinn et al., 1991; Zeebe and Lourens, 2022). Note that T_d is critical for Earth's precession and obliquity for much younger ages, but has a smaller effect on Earth's orbital eccentricity. For variations in T_d, several solutions also showed small RMSDs across depth/age Window 4 but either their e_s cycle amplitude at P28rn was weak and/or the RMSDs across Window 5 were larger than for, e.g., ZB20a and ZB20b (see Appendix B).

These results essentially left us with variations in J_2 and N_{ast} to search for viable solutions (see Table 1, for a discussion of J_2 values, see Section A.1). Around the standard values of ZB18a ($J_2 = 1.305 \times 10^{-7}$ and $N_{\mathrm{ast}} = 10$), we varied J_2 between 1.15 and 1.64×10^{-7} at $N_{\mathrm{ast}} = 10$ and N_{ast}= 10–50 at $J_2 = 1.305 \times 10^{-7}$, and some combinations of the two. Out of the resulting ensembles of solutions, we identified four solutions (Table 2, representing a certain class of solutions to ~58 Ma, see Section A.1), which showed small RMSDs and were most consistent with our selection criteria (Table 4, Fig. 1). At this stage, no preference is given to any particular solution among ZB20a, ZB20b, and ZB18a. The solutions ZB20c and ZB20d might be less preferable, given a lower J_2 and a timestep of 6 days, respectively, and a larger RMSD across Window 1 (ZB20d), 4 (ZB20c), and 5 (Table 4). Earth's orbital eccentricity for the ZB20x solutions (x = a, b, c, d), are available at www2.hawaii.edu/~zeebe/Astro.html and www.ncei.noaa.gov/access/paleo-search/study/36415. Solar system chaos and resonance transitions in relation to our astronomical solutions are discussed in Section 6.

Table 2
Properties of astronomical solutions.[a]

	Δt (days)	J_2[b] $\times 10^7$	N_{ast}	N_{LWP}
ZB18a	2	1.3050	10	0
ZB20a	2	1.4700	50	40
ZB20b	2	1.3310	10	0
ZB20c	2	1.1708	10	0
ZB20d	6	1.3050	33	33

[a] Δt = timestep, J_2= solar quadrupole moment, N_{ast}= Nº of asteroids, N_{LWP} = Nº of lightweight particles (see Appendix A).
[b] For discussion of J_2 values, see Section A.1.

3. Astronomical time scale: a simplified, initial approach

In this section, we first take a simplified approach to illustrate the construction of an ATS for the Paleocene and provide an initial evaluation of our new astronomical solutions. Based on our detailed age model (see Section 4), we concur with recent studies that the Paleocene encompasses 25 long eccentricity (405 kyr) cycles (Dinarès-Turell et al., 2014; Hilgen et al., 2010, 2015). We illustrate our simplified approach using the demeaned and detrended a^*/b^* color reflectance record at ODP Site 1262 across the Paleocene (see Fig. 2). It turned out that a^*/b^* provided a better representation of the cyclic variations in the Paleocene, compared to, e.g., a^*, which we used in the late Paleocene and early Eocene (Zeebe and Lourens, 2019). Dividing the 1262 Paleocene section into four intervals and filtering the a^*/b^* record using Gaussian filters (0.42, 0.33, 0.40, and 0.22 cycle m^{-1}, bandwidth ±50%) yielded 25 tie points for the long eccentricity cycle maxima, similar to those of Hilgen et al. (2010) (red diamonds, Fig. 2a). The four intervals are ~218-201 m, ~201-183 m, ~183-170 m, and ~170-139 m. A floating time scale based on the 405-kyr cycle is hence easily constructed. Anchoring the floating time scale at the P/E boundary with an age of 56.01 Ma (Zeebe and Lourens, 2019) then provides absolute ages for the a^*/b^* record (Fig. 2b). Next, we applied 100-kyr and 405-kyr filters to the a^*/b^* record in the time domain (Gaussian, bandwidth: ±0.0016 and ±0.0004 kyr^{-1}) and summed the two filter results. The filter sum allows direct comparison with Earth's orbital eccentricity, provided by astronomical solutions (Fig. 2c).

Furthermore, we took into account uncertainties in the inferred position of the tie points (z_{tp}), by allowing each tie point to vary by ±25 cm (5-10% of the long eccentricity cycle) and optimized z_{tp} by minimizing the root mean square deviation (RMSD) between the normalized filter sum y'_i and the normalized astronomical solution s'_i at times t_i, where $i = 1, \ldots, N_t$:

$$\mathrm{RMSD} = \left(\frac{1}{N_t} \sum (y'_i - s'_i)^2 \right)^{\frac{1}{2}} . \quad (1)$$

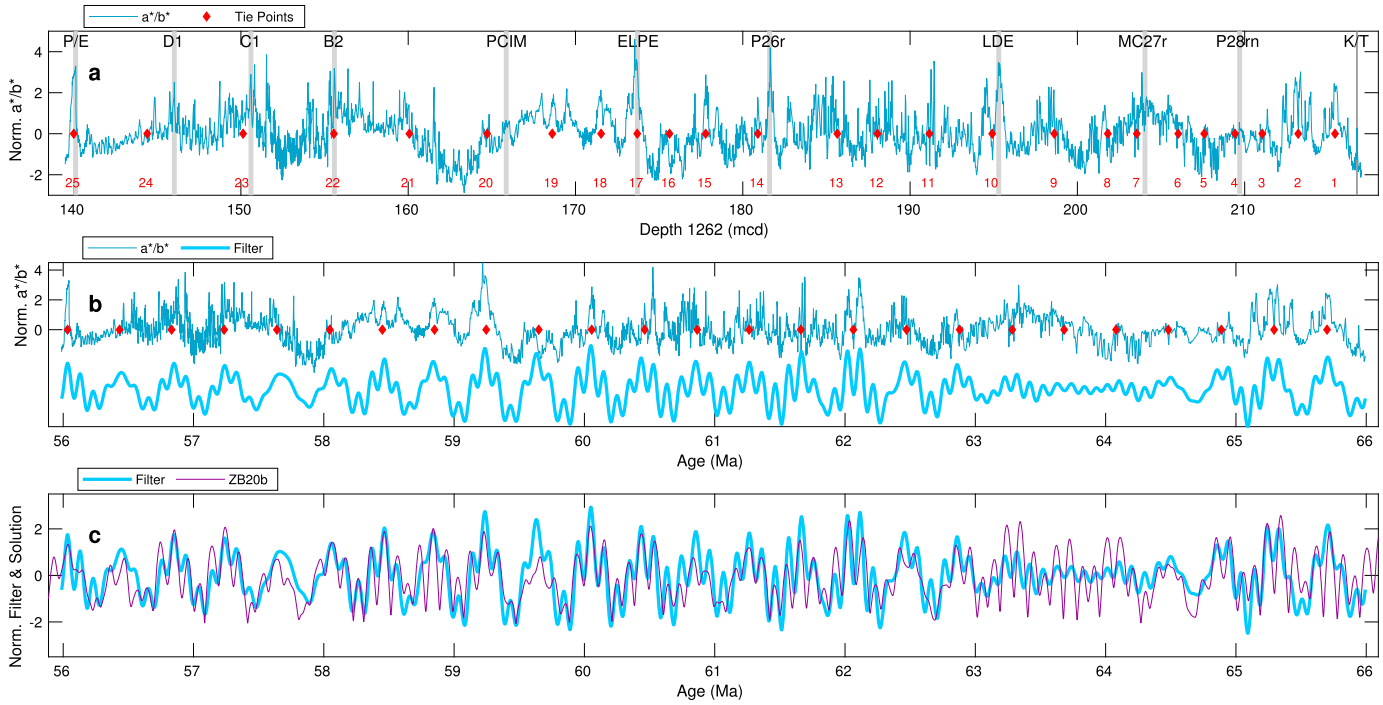

Fig. 2. Record, filter sum, and astronomical solution across the Paleocene. (a) Normalized a^*/b^* record at ODP Site 1262 in depth domain; red diamonds and numbers 1-25 indicate tie points and long orbital eccentricity cycles counted from the K/T boundary upwards (informal use, see ICS, 2005). (b) Normalized a^*/b^* record and filter sum in time domain (Gaussian, bandwidth: ± 0.0016 and ± 0.0004 kyr^{-1} for 100-kyr and 405-kyr filters). (c) Normalized filter sum and normalized astronomical solution. P/E = Paleocene-Eocene boundary, PCIM = Paleocene Carbon Isotope Maximum, ELPE = Early Late Paleocene Event, P26r = Peak Chron 26r (middle), LDE = Latest Danian Event, MC27r = Middle Chron 27r event, P28rn = Peak near C28r/C28n boundary (Site 1209), K/T = K/T boundary.

The optimization was repeated for each astronomical solution individually (for details on our new solutions, see Section 2). Finally, we evaluated the astronomical solutions using the fit (RMSD) between solution and geological record within five intervals across the Paleocene and early Eocene: 53-58, 56-58.5, 58.5-61, 61-63.5, and 63.5-66 Ma (Fig. 3). Note that the first interval (53-58 Ma) includes part of the early Eocene and overlaps with the second interval. However, including this interval as is, is important for two reasons. First, it allows direct comparison with our previous assessment of solutions (cf. Table 1 in Zeebe and Lourens, 2019). Second, given our approach, a bad fit in a well-constrained younger interval (here the early Eocene) disqualifies a solution for all older intervals (here the Paleocene, for further discussion, see Section 4).

The results of our initial assessment of various astronomical solutions show a few robust trends (see Fig. 3). For example, overall the ZBx solutions ($x = 18$a and 20abcd, this study and Zeebe and Lourens (2019)) show generally better agreement with the 1262 records than the Lax solutions ($x = 10$abcd and 11) (Laskar et al., 2011a,b). This result is not surprising, given the selection of our new solutions (see Section 2). Importantly, while La10d, for instance, provides a good match from 56-58.5 Ma, overall the solution is not a good fit because of the large RMSDs in other intervals. Of the five Lax solutions, La10b and La10c provide the best fits (consistent with earlier work, see Westerhold et al. (2017); Zeebe and Lourens (2019)) but have larger RMSDs than the ZBx solutions in most intervals.

Our initial solution assessment (Fig. 3) illustrates another important point. Unfortunately, small RMSD differences between solutions in a given time interval are not a robust criterion for solution selection. For instance, if we use the 1262-Fe record (Fig. 3c and d) instead of a^*/b^* (Fig. 3a and b), the results are slightly different. For example, in the two oldest intervals, the solution ZB20b provides a better fit to the Fe record than to the a^*/b^* record. Thus, concluding that ZB20b performs worse than, e.g., ZB20d solely based on a^*/b^* would be premature, as their ranking is reversed when considering the Fe record. As a result, while the overall trends of our initial assessment are likely robust, the details are not, and depend on a variety of factors, including the proxy record used, filtering, tie point position, etc. Additional criteria are therefore required for robust solution selection.

4. Astronomical time scale: ODP Sites 1262/1209 and Zumaia

In this section, we take a more detailed approach and develop an age model based on cyclostratigraphy from ODP Sites 1262/1209 and Zumaia, in some instances considering features at the resolution of the 100-kyr cycle (Dinarès-Turell et al., 2014; Hilgen et al., 2010, 2015). Importantly, our general approach presented in Zeebe and Lourens (2019) and here extends the astronomical time scale working backwards from younger to older sections and hence requires suitable fits not only in a given, but in all younger, intervals. Given that approach, a bad fit in a well-constrained younger interval thus disqualifies a solution for all older intervals, regardless of whether that solution may provide a good fit to an older section of the record. Misfits in the oldest interval may potentially be improved by further (smaller) parameter variations starting with a given solution, but not misfits in a younger interval.

4.1. Depth/age windows

For our detailed age model, we used six separate windows in which we applied filters to the 1262 and 1209 Fe records (see Fig. 4, Table 3). For multi-million year records, multiple windows are usually inevitable, for instance, because of changes in sedimentation rates, condensed sections, large events that result in filter distortion, and more (a single record very rarely shows a homogeneous pattern, say, across ~10 Myr or so). For most of the Paleocene, we used the proxy records at Site 1262, which showed well-developed cyclic variations, superior to, e.g., those

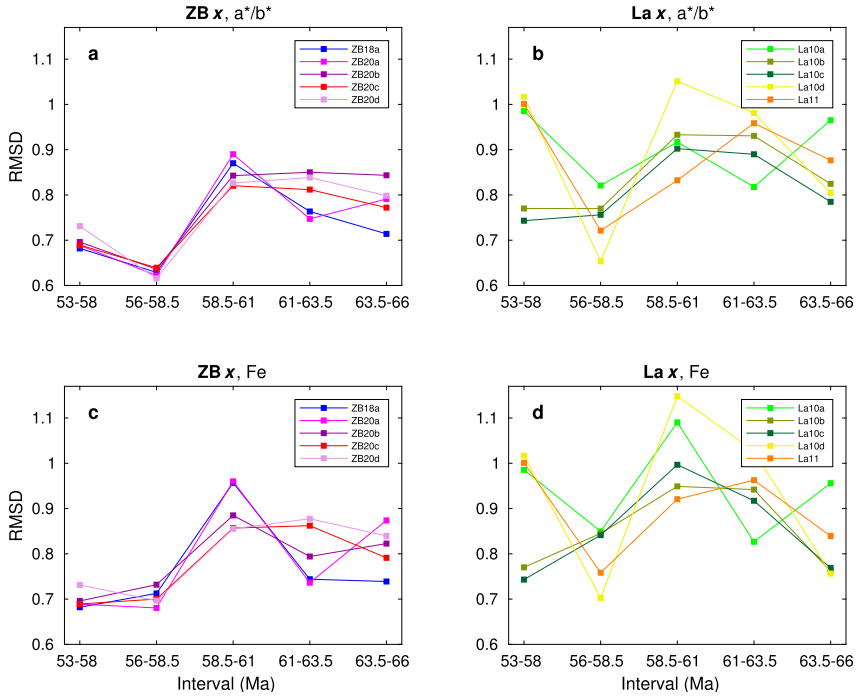

Fig. 3. Root mean square deviations (RMSDs) between normalized, filtered proxy records (ODP Site 1262) and normalized astronomical solutions (ZB*x* and La*x*) across different time intervals (abscissa). (a) and (b) using the a^*/b^* proxy record. (c) and (d) using the Fe proxy record.

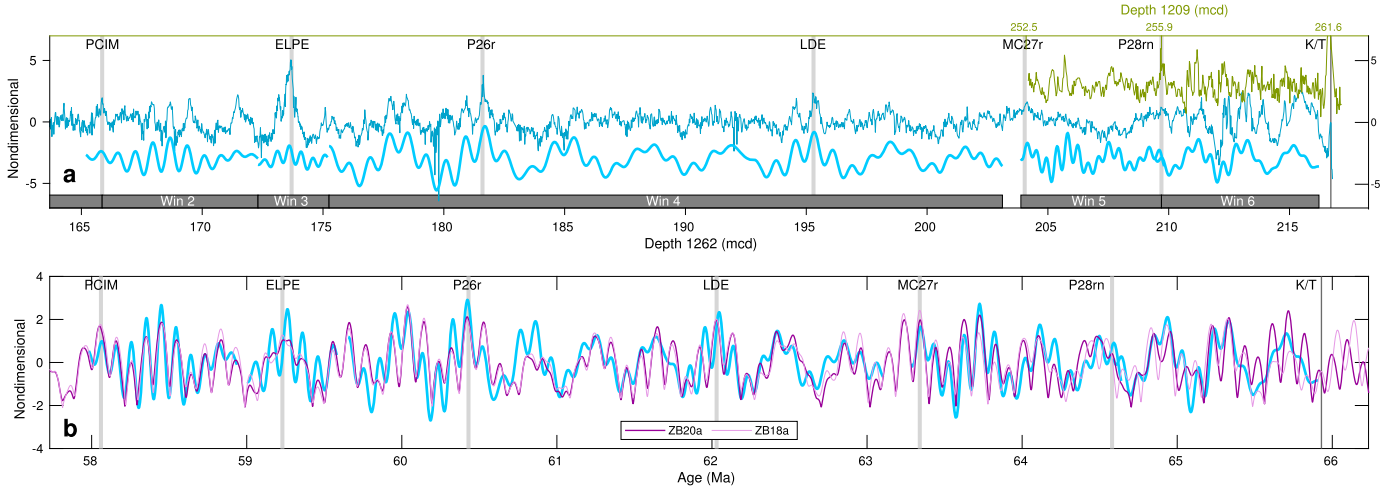

Fig. 4. Records, depth/age windows, and astronomical solutions from ~66 to ~58 Ma (see Appendix B for details). (a) Demeaned, detrended, and normalized Fe records at ODP Sites 1262 (blue-gray), 1209 (olive), and filter output (light blue) with arbitrary offsets. Horizontal bars indicate intervals of windows; the filter output and age model is based on Site 1262 for Windows 1-4 and on Site 1209 for Windows 5 and 6 (see Appendix B and Table 3). (b) Normalized filter sum (blue) and normalized astronomical solutions (purple and light purple). PCIM = Paleocene Carbon Isotope Maximum, ELPE = Early Late Paleocene Event, P26r = Peak Chron 26r (middle), LDE = Latest Danian Event, MC27r = Middle Chron 27r event, P28rn = Peak near C28r/C28n boundary (Site 1209), K/T = K/T boundary (informal use, see ICS, 2005).

at Site 1209, which also has a lower average sedimentation rate (~0.4 cm kyr^{-1}) than Site 1262 (~0.8 cm kyr^{-1}). However, efforts to obtain a filtered Fe record at Site 1262 for the interval across Windows 5 and 6 consistent with the Zumaia record and Site 1209 were unsuccessful (see Appendix B and Table 3). Hence we used the Fe record at Site 1209 for Windows 5 and 6. As mentioned above, our approach works backwards from younger to older sections, hence the window order is most recent first.

Window 1 covers the late Paleocene and early Eocene, corresponding to the first interval of our simplified approach (see Section 3), which was studied in detail by Zeebe and Lourens (2019). Windows 2 and 3 are relatively short and unproblematic — accordingly, our analysis yielded results in agreement with earlier work (Dinarès-Turell et al., 2014; Hilgen et al., 2010, 2015; Westerhold et al., 2008). The ELPE (Window 3) is treated separately because of its large signal amplitude, which causes filter distortion. However, the window is short and hence the mismatch between filter and astronomical solution in terms of RMSD is not critical. Windows 4-6 cover sections that are more complex, the details of which are discussed in Appendix B. In our evaluation of solutions using RMSDs for different windows, we will primarily give consideration to Windows 1, 4, 5 and 6, rather than to Windows 2 and 3.

One important feature of the records to keep in mind at this point is a reduced short eccentricity amplitude in Window 4 between P26r and the LDE, i.e., around 185-192 meters composite depth (mcd) at Site 1262, roughly corresponding to an age of ~61 Ma (see Fig. 4). This feature is apparent in the Fe, benthic δ^{13}C, and a^*/b^* proxy records at Site 1262 (although more promi-

Table 3
Depth/age windows.

Window	Core	Interval[a]	Filter[b] (cycle m^{-1})	Depth (mcd)[c]	Age[d] (Ma)
1	1262	[I2,PCIM]	0.20, 0.80[e]	112.43-165.86	53.56-58.06
2	1262	[PCIM,ELPE)	0.33, 1.34	165.20-172.30	57.98-58.94
3	1262	[ELPE]	0.50, 2.00	172.30-175.20	59.00-59.58
4	1262	(ELPE,MC27r)	0.29, 1.25	175.24-202.50	59.65-63.10
5	1209	[MC27r,P28rn]	0.86, 3.45	252.40-256.00	63.28-64.64
6	1209	[P28rn,K/T)	0.59, 2.50	255.70-261.20	64.59-65.91

[a] Brackets and parentheses indicate intervals with endpoints included and excluded, respectively. I2 = Eocene thermal event I2 (see e.g., Lauretano et al., 2016). PCIM = Paleocene Carbon Isotope Maximum, ELPE = Early Late Paleocene Event, MC27r = Middle Chron 27r event, P28rn = Peak near C28r/C28n boundary (Site 1209), K/T = K/T boundary.
[b] Center frequency for long, short eccentricity filter (Gaussian, bandwidth ±20%).
[c] Meters composite depth.
[d] Interval ages for Window 1 are event tie points (cf. Supplement of Zeebe and Lourens, 2019). Interval ages for Window 2-6 (based on ZB20a) are filter boundaries (not event tie points) and may overlap for consecutive windows (see text).
[e] 140.12-165.86 m. For in-depth analysis of the interval 112.43-140.12 m, see Zeebe and Lourens (2019).

nent in Fe than a^*/b^*, cf. Fig. 2a), as well as at Site 1209. We therefore consider the reduced short eccentricity amplitude around 61 Ma a robust feature, which prompts us to search for very long eccentricity nodes around this time in the astronomical solutions (see below).

4.2. Window summary

Our detailed age model yields results similar to our simplified approach (Section 3) but adds additional constraints and selection criteria for astronomical solutions (Fig. 4 and Table 4). These criteria include existence of a very long eccentricity node around 61 Ma (see above) and the solution's cycle amplitude at MC27r and P28rn (see Appendix B for details, Table 4 for summary). The RMSD results are consistent with those of our simplified approach, indicating that the ZB*x* solutions perform better than the La*x* solutions (again, not surprising given the selection of the ZB*x* solutions, see Section 2). For completeness, we have also included La10a, La10d, and La11 in the detailed analysis, despite their mismatch in the late Paleocene and early Eocene (Window 1, see Fig. 3). In addition, La11 has been previously used to reconstruct a Paleocene ATS and determine the K/T boundary age (Dinarès-Turell et al., 2014; Hilgen et al., 2015).

Importantly, while La10b and La10c do show low RMSDs across Window 1, these solutions do not exhibit very long eccentricity nodes around 61 Ma (which we consider a robust feature of the records, however, see Section 4.1). As a result, the La*x* solutions are less preferable than the ZB*x* solutions. As mentioned above, no preference is given to any particular solution among ZB20a, ZB20b, and ZB18a. The solutions ZB20c and ZB20d might be less preferable, given a lower J_2 and a timestep of $\Delta t = 6$ days, respectively (compared to the standard $\Delta t = 2$ days, see Section 2), and a larger RMSD across Window 1 (ZB20d), 4 (ZB20c), and 5 (Table 4).

5. K/T boundary age

The K/T boundary (informal use, see ICS, 2005) appears to occur close to a long eccentricity (405 kyr) minimum, i.e., below the 25th 405-kyr maximum counted from (and including) the P/E boundary downwards (see Figs. 2 and B.2). More precisely, Kuiper et al. (2008) defined the astronomical K/T boundary age by placing the boundary ∼2.5 precession-related cycles below the oldest (Paleocene) tuned 100-kyr eccentricity minimum, using an average precession period of 21 kyr at that time (see Fig. B.2). Dinarès-Turell et al. (2014) defined the astronomical K/T boundary age by placing the boundary ∼3.5 precession cycles above the youngest (Cretaceous) tuned 100-kyr eccentricity maximum (consistent with Gilabert et al. (2022), see also Fig. 3 in Batenburg et al. (2012)). Here, the subsequent (younger, not older) e_s minimum is assigned the same number as a given e_s maximum. Cretaceous e_s maxima are assigned negative numbers (see Fig. B.2). For the two options we can then write:

$$t_{KT_1} \simeq t_{e_s(min_1)} + 2.5 \times 21 \text{ kyr} \quad (2)$$

$$t_{KT_2} \simeq t_{e_s(max_{-1})} - 3.5 \times 21 \text{ kyr}\,, \quad (3)$$

which yield similar results, differing by ∼10 kyr for most of the solutions tested here (see Table 4).

More importantly, because the g_2–g_5 cycle (∼405 kyr, see Section 6) differs slightly between astronomical solutions, the age model and hence the inferred K/T boundary age depends on the astronomical solution used for tuning (Table 4). One of the factors influencing the g_2–g_5 cycle are potential resonance transitions due to solar system chaos, which can occur for ages older than ∼50 Ma (see Section 6). As a result, there is a relationship, for instance, between the g_2–g_5 cycle at ∼66 Ma and the behavior of a solution around 50 Ma. For example, the solutions ZB18a, ZB20*x*, La10b, and La10c all indicate slightly younger K/T boundary ages (see Fig. 5 and Table B.1). At the same time, all these solutions show a similar resonance transition pattern around 50 Ma (see Section 6), which yields relatively small RMSDs across Window 1. In contrast, the solutions ZB17a, La10d, and La11 all indicate slightly older K/T boundary ages (La10a falls somewhat off the trend, see Fig. 5). These solutions show a different (or no) resonance transition pattern around 50 Ma, which yields relatively large RMSDs across Window 1. As a result, there is a relationship between the Window 1-RMSD and the astronomical K/T boundary age of a solution (Fig. 5).

The different inferred astronomical K/T boundary ages are a direct result of the g_2–g_5 cycle of the different solutions and hence correlate with the solutions' ages of the first (oldest) Paleocene long-eccentricity minimum (Table B.1). Within errors, the K/T boundary ages based on the solutions ZB20c and ZB20d are consistent with recent radiometric ages from U-Pb dating (Clyde et al., 2016) (see Fig. 5). Relative to $^{40}Ar/^{39}Ar$ ages (Renne et al., 2013; Sprain et al., 2018), the K/T boundary ages based on the preferred solutions ZB20a, ZB20b, and ZB18a fall between two different calibrations that have been applied to the $^{40}Ar/^{39}Ar$ data (A: Kuiper et al., 2008) and most recently (B: Renne et al., 2011), see also Schaen et al. (2020). Our astronomical ZB*x*-K/T ages (∼65.92-65.96 Ma) are up to ∼70 kyr older and up to ∼90 kyr younger than the reported upper and lower error bounds for the $^{40}Ar/^{39}Ar$ calibration A and B (most recent), respectively. While the K/T boundary

Table 4
RMSD[a], selection criteria, and K/T age for astronomical solutions.[b]

	Win 1 RMSD	Win 4[c] RMSD	Win 5 RMSD	Win 6 RMSD	Node[d]	Cycle Nº[e]	Cycle amp[f]	K/T age (Ma)[g]
ZB18a	0.6820	0.8897	0.8835	0.6906	Y	27/14	s/m	65.94/65.96
ZB20a	0.6888	0.8862	0.8072	0.8343	Y	28/15	s/m	65.92/65.92
ZB20b	0.6959	0.8518	0.7950	0.8757	Y	28/15	s/m	65.92/65.93
ZB20c	0.6892	0.9304	0.9335	0.6716	Y	27/14	s/m	65.95/65.96
ZB20d	0.7312	0.8974	**0.9927**	0.7353	Y	27/14	s/m	65.95/65.95
La10a	0.9854	0.9582	0.7804	0.9725	Y	?[h]	?	65.96/65.95
La10b	0.7702	0.9117	0.7717	0.6510	**N**	27/14	**s/w**	65.95/65.96
La10c	0.7431	0.9444	0.9661	0.6619	**N**	27/14	s/m	65.95/65.96
La10d	**1.0320**	**1.0085**	0.7092	0.9221	Y	?[h]	?	66.01/66.01
La11	**1.0009**	**1.0003**	0.7612	0.9046	**N**	28/15	s/s	66.01/66.02

[a] Root mean square deviation between normalized solution and normalized filtered record.
[b] RMSDs > 0.99 and compatibility issues with selection criteria are marked in **bold**. Win = Window.
[c] La*x* solutions in Win 4 are offset by one e_s cycle relative to ZB*x* (yields smaller RMSDs for La*x*).
[d] Very long eccentricity node around 61 Ma (Yes/No).
[e] Short eccentricity cycle Nº at MC27r/P28rn (counted from the K/T boundary upwards, see Fig. B.2).
[f] Short eccentricity cycle amplitude at MC27r/P28rn: s/m/w = strong/intermediate/weak.
[g] Eq. (2)/Eq. (3).
[h] Short eccentricity cycle assignment ambiguous.

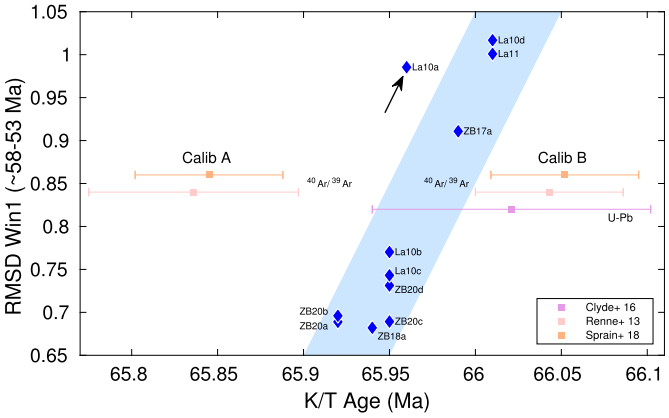

Fig. 5. Root mean square deviation (RMSD, Window 1) vs. K/T boundary age. The Win 1-RMSD between record and astronomical solution vs. astronomical K/T boundary age (diamonds) falls generally on an increasing trend (blue shaded area), La10a falls off the trend (arrow). Squares and error bars indicate recent radiometric K/T boundary ages based on U-Pb (Clyde et al., 2016) and $^{40}Ar/^{39}Ar$ (Renne et al., 2013; Sprain et al., 2018) with two different calibrations (A: Kuiper et al., 2008), (B: Renne et al., 2011) for $^{40}Ar/^{39}Ar$ (cf. Schaen et al., 2020).

ages based on the solutions La10d and La11 appear consistent with $^{40}Ar/^{39}Ar$ calibration B and the U-Pb ages, we consider those unlikely because of the misfit of these solutions to geological data across the Paleocene and early Eocene (Table 4).

6. Chaos and resonance transitions

The sensitivity of astronomical solutions to initial conditions and small parameter variations is a critical ingredient for the chaotic behavior of the solar system (e.g., Sussman and Wisdom, 1988; Laskar, 1989; Nobili et al., 1989; Laskar, 1990; Sussman and Wisdom, 1992). As a result, many astronomical solutions start showing discernible differences for ages older than ~50 Ma (e.g., Laskar et al., 2011a; Zeebe, 2017; Zeebe and Lourens, 2019). Small variations in a single parameter as tested here, for instance, $\Delta J_2 = 0.16 \times 10^{-7}$, leads to a clear shift in the very long eccentricity nodes (VLNs) in the solutions ZB20b and ZB20c by about one 405-kyr cycle around 59 Ma (long eccentricity cycle Nº 16 vs. 17, see Fig. 1). To compare a number of different solutions, such shifts may be summarized by the time interval (Δ_{vln}) between consecutive minima in a 2-Myr filter of eccentricity (Gaussian, bandwidth ±60%), which approximately coincides with the interval between VLNs (Zeebe and Lourens, 2019) (see Fig. 6). Plotting, for instance, the preceding (older) interval Δ_{vln} at the age of the filter minimum (as in Fig. 6) also allows a comparison of the ages of the VLNs for different solutions.

As expected by the selection of the ZB20*x* and ZB18a solutions (see Section 2), their Δ_{vln} are virtually identical after ~56 Ma (Fig. 6a). Between ~66 Ma and ~56 Ma, their Δ_{vln} differ, roughly corresponding to the VLNs highlighted in Fig. 1, and within certain bounds ($\Delta_{vln} \simeq 1.2$ to 2.0 Myr). Note that ZB20a, ZB20b, and ZB20c show VLNs very close to 61 Ma (Fig. 6a, vertical line), which is one of our selection criteria for viable solutions (see Table 4). In contrast, for the La10*x* and La11 solutions, the Δ_{vln} diverge around 48 Ma and show larger differences between ~66 Ma and ~56 Ma ($\Delta_{vln} \simeq 1.0$ to 2.4 Myr, Fig. 6b). Importantly, La10b and La10c show a pattern similar to ZB20*x* and ZB18a after ~54 Ma (Fig. 6, arrows), corresponding to a relatively small RMSD across Window 1 (see Table 4). However, these solutions do not show VLNs at 61 Ma (Fig. 6b, vertical line), but rather at about 60 and 62 Ma (note that the VLN requirement at 61 Ma is based on a robust feature of the records, see Section 4.1). La10a and La10d, which do show VLNs close to 61 Ma, have pattern different from ZB20*x* and ZB18a after ~54 Ma, corresponding to large RMSDs across Window 1.

The examination of the Δ_{vln} above illustrates the difficulty in finding adequate solutions to match the geologic record. A given solution might be a good fit across a certain interval, but a bad fit across another. Importantly, given the current approach, a bad fit in a well-constrained younger interval disqualifies a solution for all older intervals, regardless of whether that solution may provide a good fit to an older section of the record (see Section 4). Δ_{vln} also illustrates the chaotic behavior of the solar system. For example, the steady rise in Δ_{vln} between ~53 and ~45 Ma in ZB20*x* and ZB18a is called a resonance transition, which is an unmistakable manifestation of chaos and is also key to distinguishing between different solutions before ~50 Ma (Zeebe and Lourens, 2019). Given the currently available records, at this time it appears that solutions with Δ_{vln} and resonance pattern such as ZB20a, ZB20b, ZB20c, and ZB18a are most suitable for constructing an astronomically-tuned time scale for the Paleocene. However, this may change as new geologic records become available.

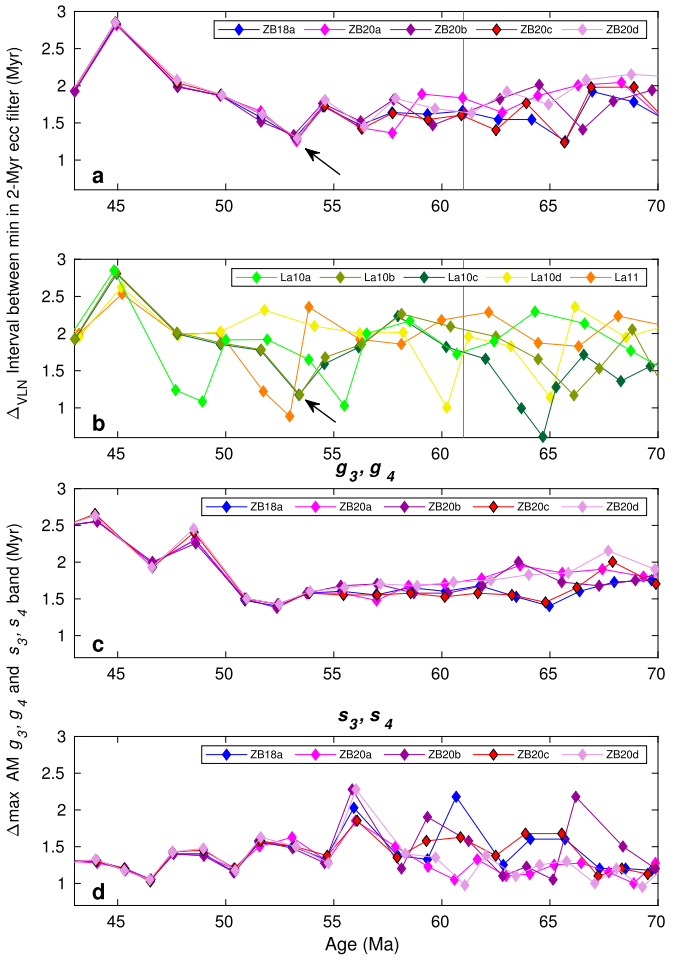

Fig. 6. (a, b) Time interval (Δ_{vln}) between consecutive minima in a 2-Myr filter of eccentricity (Gaussian, bandwidth ±60%) for different astronomical solutions: (a) ZB*x*, (b) La*x*. Δ_{vln} approximately coincides with the interval between very long eccentricity nodes (VLNs) (see Fig. 1). The solutions ZB20*x* and La10b and c behave similar around 54 Ma (arrows). In contrast, ZB20a, b, and c have VLNs very close to 61 Ma, whereas La10b and c do not (vertical lines). (c, d) Time interval (Δmax) between consecutive maxima in the amplitude modulation (AM) of frequencies in the band around (c) [g_3, g_4] and (d) [s_3, s_4] based on spectral analysis (evolutive harmonic analysis) of the variables h and p (see Eq. (4)) for different astronomical solutions (ZB*x*). Note the transition from ~1.5 Myr to $\gtrsim$2.0 Myr around 50 Ma in the g-modes (c), whereas no such transition occurs in the s-modes around that time (d).

6.1. Resonance transition and solar system frequencies

The resonance transition between ~53 and ~45 Ma, causing changes in the very long eccentricity nodes, is associated with so-called g-modes (fundamental solar system frequencies such as g_3 and g_4, loosely related to the perihelion precession of Earth's and Mars' orbits) and is a macroscopic feature that can be observed in the geologic data (Zeebe and Lourens, 2019). A complete check on resonance transitions would strictly also require examination of s-modes in the geologic record (which mirrors the actual solar system), e.g., frequencies s_3 and s_4 (e.g., Ma et al., 2017; Pälike et al., 2004; Westerhold et al., 2017), which are loosely related to the nodes of Earth's and Mars' orbits (see e.g., Laskar et al., 2011a; Zeebe, 2017; Zeebe and Lourens, 2019). However, evaluating g- and s-modes simultaneously is often difficult as it usually requires good signals of precession/eccentricity, as well as obliquity. For the Paleocene, we have focused on eccentricity records here (g_4–g_3), as we are unaware of suitable obliquity records (see Appendix C), which would also allow us to examine s_4–s_3 in the geologic record. However, we can examine s_4–s_3 in our astronomical solutions and ask, for instance, whether certain changes in g_4–g_3 are sufficient to indicate a resonance transition, without detailed knowledge of changes in s_4–s_3.

In our solutions ZB20*x* and ZB18a, the period associated with g_4–g_3 switches from ~1.5 Myr to ~2.4 Myr between ~53 and ~45 Ma, consistent with the geologic record, i.e., interpretation of strata that span this interval (Westerhold et al., 2017; Zeebe and Lourens, 2019). The ratio $(g_4\text{–}g_3) : (s_4\text{–}s_3)$ is about 1 : 1 in our solutions before the onset of the transition around 53 Ma (one resonance state) and about 1 : 2 after the transition around 45 Ma (another resonance state, see Fig. 6c and d). The resonance transition hence occurs during the interval from ~53 to ~45 Ma when the system switches from one resonance state to another. This time interval is accordingly referred to as transition interval, not the interval prior to ~53 Ma. If a switch in the $(g_4\text{–}g_3) : (s_4\text{–}s_3)$ ratio indicates a resonance transition (and conversely, constancy indicates absence), then the g_4–g_3 switch also indicates a resonance transition, unless s_4–s_3 in the actual solar system would switch simultaneously from ~0.75 Myr to ~1.2 Myr between ~53 and ~45 Ma to keep the ratio constant (not the case of course in our solutions, see Fig. 6). To the best of our knowledge, such a resonance behavior has never been proposed theoretically (e.g., Sussman and Wisdom, 1992; Laskar et al., 2011a). Neither have we found any intervals with values as low as ~0.75 Myr for s_4–s_3 at all in over 160 solar system integrations we examined, including ZB20*x* and ZB18a (Fig. 6d). This strongly suggests that the g_4–g_3 switch between ~53 and ~45 Ma indeed indicates a resonance transition in the solar system. One future task to perform if/when appropriate geologic data for s_4–s_3 becomes available is to check whether the resonance transition occurs from a ratio of ~1:1, or a different ratio, to ~1:2 around 50 Ma.

To examine changes in $(g_4\text{–}g_3) : (s_4\text{–}s_3)$ in our solutions, we analyzed the amplitude modulation (AM) in the frequency bands around periods of ~70–75 kyr (g_3, g_4) and ~68–74 kyr (s_3, s_4) in the respective variables (e.g., Nobili et al., 1989; Zeebe and Lourens, 2019):

$$h = e \sin \varpi \quad ; \quad p = \sin(I/2) \sin \Omega \,, \tag{4}$$

where e, I, ϖ, and Ω are eccentricity, inclination, longitude of perihelion, and longitude of ascending node of Earth's orbit, respectively (Fig. 6). Note that wavelet analysis (Zeebe and Lourens, 2019) and evolutive harmonic analysis (e.g., Meyers, 2014) yielded similar results. For cyclostratigraphic purposes, different analyses tools are of course required, as h- and p-time series are not available from the geologic record. For the ZB20*x* and ZB18a solutions, the pattern for the time interval between consecutive maxima in the AM of the [g_3, g_4] frequency band (indicative of g_4–g_3, Fig. 6c) is similar to that of Δ_{vln} (Fig. 6a), only that Δ_{vln} is defined using just eccentricity and consecutive minima, rather than maxima. Again, note the prominent switch from ~1.5 Myr to $\gtrsim$2.0 Myr around 50 Ma (Fig. 6c). No prominent shifts occur around that time in the corresponding [s_3, s_4] frequency band (indicative of s_4–s_3, Fig. 6d), demonstrating that a resonance transition indeed occurs in the ZB20*x* and ZB18a solutions around 50 Ma. The pattern for s_4–s_3 before the transition is more irregular, the details of which somewhat depend on parameters and tools used for spectral analysis though. If anything, the period associated with s_4–s_3 shows several larger values before ~55 Ma, corresponding to smaller frequency values of $|s_4\text{–}s_3|$. The tendency to smaller $|s_4\text{–}s_3|$ values before ~55 Ma was confirmed by a direct fast Fourier transform of p (see Eq. (4)) across 10 Myr windows, with the change in s_4–s_3 mostly driven by s_3.

6.2. The age of the youngest resonance transition and the nature of chaos

The youngest resonance transition in the ZB20*x* and ZB18a solutions is not abrupt but occurs over several million years. Hence no single, precisely defined age can be given for the transition. Our analysis of Earth's eccentricity and g_4–g_3 suggest the transition to occur across the interval from ∼53 to ∼45 Ma (see Fig. 6). This time interval is broadly consistent with the wavelet analysis presented in Fig. 2 of Zeebe and Lourens (2019). However, we emphasize that due to the gradual nature of the transition, the interval is not well-defined and also depends somewhat on the variable and method selected for the analysis. Nevertheless, significantly younger transition ages as suggested by the La04 solution (Laskar et al., 2004) are not supported by our ZB20*x* and ZB18a solutions. In fact, La04 disagrees with the more recent solutions ZB17*x*, ZB18a, ZB20*x*, La10*x*, and La11 already around 41 Ma (Zeebe, 2017); the use of La04 is therefore not recommended prior to that age.

Resonance transitions are also referred to as chaotic transitions because they are characteristic indicators for chaos in certain dynamical systems (note that one critical ingredient for chaos is the sensitivity to initial conditions). While, for instance, resonance transitions in astronomical solutions may occur only across a limited time interval, the chaos inherent in the system is a fundamental property affecting its behavior in general (not only across a transition). Hence the notion that chaos would "act" only over a limited time period to cause the resonance transition or the divergence of solutions at a specific point in time (see e.g., Fig. 6a around 56 Ma) is a misconception. The resonance transition and divergence of solutions are both expressions of the system's inherent and continuous chaos (Lyapunov time ∼5 Myr in the inner solar system). It is just that the divergence of solutions, for example, is revealed macroscopically only after many Lyapunov times, here on time scales exceeding 50 Myr or so.

7. Summary and conclusions

We have introduced a new set of astronomical solutions to extend the fully calibrated astronomical time scale across the Paleocene, following Zeebe and Lourens (2019). The solutions are available to 300 Ma (www2.hawaii.edu/~zeebe/Astro.html, www.ncei.noaa.gov/access/paleo-search/study/36415); we caution, however, that the time interval 300-66 Ma is unconstrained due to dynamical chaos in the solar system. Our orbital solutions provide better fits to Paleocene data records (ODP Sites 1262 and 1209) than previously available solutions. Given the currently available records, at this time it appears that solutions with properties and chaotic resonance pattern such as ZB20a, ZB20b, and ZB18a are most suitable for constructing an astronomically-tuned time scale for the Paleocene. However, these conclusions may change as new geologic records become available. The K/T boundary (KTB) ages obtained using our new solutions suggest slightly younger KTB ages than those inferred from most recent $^{40}Ar/^{39}Ar$ radiometric dating.

CRediT authorship contribution statement

Richard E. Zeebe: Conceptualization, Investigation, Methodology, Software, Writing – original draft. **Lucas J. Lourens:** Investigation, Methodology, Writing – review & editing.

Declaration of competing interest

The authors declare that they have no known competing financial interests or personal relationships that could have appeared to influence the work reported in this paper.

Data availability

Earth's orbital eccentricity for the ZB20*x* solutions is available at www2.hawaii.edu/~zeebe/Astro.html and www.ncei.noaa.gov/access/paleo-search/study/36415.

Acknowledgements

We thank the reviewers Linda Hinnov and Slah Boulila for suggestions, which have improved the manuscript. This research was supported by U.S. NSF grants OCE20-01022, OCE20-34660 and Heising-Simons Foundation Grant #2021-2800 to R.E.Z. and grants from the Netherlands Organisation for Scientific Research (NWO-ALW 865.10.001) and the Netherlands Earth System Science Centre (NESSC 024.002.001) to L.J.L.

Appendix A. Solar system integrations

Solar system integrations were performed following our earlier work (Zeebe, 2015a,b, 2017; Zeebe and Lourens, 2019) with the integrator package `HNBody` (Rauch and Hamilton, 2002) (`v1.0.10`) using the symplectic integrator and Jacobi coordinates (Zeebe, 2015a). All simulations include contributions from general relativity (Einstein, 1916), available in `HNBody` as Post-Newtonian effects due to the dominant mass. The Earth-Moon system was modeled as a gravitational quadrupole (Quinn et al., 1991) (`lunar` option), shown to be consistent with expensive Bulirsch-Stoer integrations up to 63 Ma (Zeebe, 2017). Initial conditions for the positions and velocities of the planets and Pluto were generated from the JPL DE431 ephemeris (Folkner et al., 2014) (naif.jpl.nasa.gov/pub/naif/generic_kernels/spk/planets), using the SPICE toolkit for Matlab (naif.jpl.nasa.gov/naif/toolkit.html). We also tested the latest JPL ephemeris DE441 (Park et al., 2021), which has a small effect on the results, i.e., the divergence time relative to ZB18a (based on DE431) is $\tau \simeq 66$ Ma. For consistency with ZB18a, we used DE431 for our new solutions (ZB20*x*) presented here. For INPOP08a (www.imcce.fr/inpop), initial conditions were generated using the calceph library in C (www.imcce.fr/inpop/calceph). The integrations for ZB20*x* (ZB = **Z**eebe-HN**B**ody) included different numbers of asteroids (N_{ast}, see Table 2), with initial conditions generated at ssd.jpl.nasa.gov/x/spk.html (for a list of asteroids, see Zeebe (2017)). Sets of asteroids were either treated as heavyweight particles (HWPs) or lightweight particles (LWPs) in `HNBody` (Table 2). HWPs are subject to the same full interactions as the planets. LWPs are dynamically equivalent to HWPs but self-gravity (LWP-LWP forces) is ignored; HWP-LWP interactions are included (see Rauch and Hamilton, 2002). Coordinates were obtained at JD2451545.0 in the ECLIPJ2000 reference frame and subsequently rotated to account for the solar quadrupole moment (J_2) alignment with the solar rotation axis (Zeebe, 2017). Earth's orbital eccentricity for the ZB20*x* solutions is available at www2.hawaii.edu/~zeebe/Astro.html and www.ncei.noaa.gov/access/paleo-search/study/36415. We provide most of our solutions over the time interval from 100-0 Ma (ZB18a and ZB20*x* over 300-0 Ma). However, as we only provide an analysis for the Paleocene/Cenozoic here, we caution that the interval prior to 66 Ma is unconstrained due to solar system chaos.

A.1. Solar quadrupole moment J_2

The J_2 value of $\sim 1.3\text{-}1.5 \times 10^{-7}$ used in several of our preferred solutions is lower than 2.2×10^{-7} used in our earlier work (Zeebe, 2017), where the latter is based on recent (modern) evidence (Park et al., 2017; Pijpers, 1998). However, as described in the Supplement of Zeebe and Lourens (2019), J_2 can be increased in the simulations with a larger asteroid population (N) to yield very similar

solutions up to a certain age (we refer to a set of such similar solutions as a "class" of solutions). We have only tested up to $N = 50$, while current ephemerides may include $N > 300$, and in reality N may be $>10^6$ with size >1 km (though only a small fraction of this is dynamically relevant). Nevertheless, given that $N = 50$ corresponds to $J_2 \simeq 1.5 \times 10^{-7}$, perhaps $J_2 \simeq 1.8 - 2.0 \times 10^{-7}$ is feasible with a larger asteroid population (note, however, that 100-Myr integrations with large N are computationally still very expensive). Thus, it is possible that the J_2 value used in long-term integrations can be reconciled with modern evidence if a large asteroid population is included. Another possibility is that parameters required for long-term integrations that are compatible with geologic observations of the past are not fully compatible with our best knowledge of the current solar system. Note in this context that the La10c solution (Laskar et al., 2011a) with a small Win-1 RMSD (see Table 4) used the INPOP08 ephemeris (Fienga et al., 2009), which is considered less accurate than more recent versions such as INPOP10 used for La11. Yet, La10c fits the geologic data better than La11 (see Table 4, and Westerhold et al., 2017).

Appendix B. Depth/age windows of detailed age model

In this Appendix we discuss Windows 4-6 of the detailed age model (for Windows 1-3, see Section 4.1). Regarding RMSDs (see Table 4), note that some solutions showed two similarly small RMSDs that were usually offset by one short eccentricity (e_s) cycle between the solution and the filter. Unless stated otherwise, the reported RMSD corresponds to the e_s position consistent with the window interval ages given in Table 3. In the following, H15 = Hilgen et al. (2015), D14 = Dinarès-Turell et al. (2014).

B.1. Window 4: ELPE to MC27r

Spectral analysis of the Fe record at Site 1262 showed a relatively homogeneous cycle pattern between the ELPE and MC27r (~175 to ~204 m). Excluding the long eccentricity cycles (e_l) encompassing the ELPE and MC27r, our Fe filter yields nine e_l for this section, in agreement with previous work (e.g., Barnet et al., 2019; Westerhold et al., 2008). The section below ~190 m is also nearly consistent with the available record at Zumaia for the early Paleocene [H15; D14], with one exception. Within the ~1.5 m above MC27r our filter at Site 1262 indicated one short eccentricity maximum ($1 \times e_s$), whereas the stratigraphic record at Zumaia (and Site 1209) indicate $2 \times e_s$ [H15; D14]. This suggests a somewhat reduced sedimentation rate (and/or condensed section) for the interval just above MC27r at Site 1262. As a result, the window interval was terminated at 202.5 m (instead of 204 m) to avoid the problematic bottom 1.5 m. In addition, the interval between 198.5 m and 202.5 m was stretched, which resulted in a better match with long- and short eccentricity cycles, when compared to the interval above and to astronomical solutions across the interval. The stretch did not alter the total number of e_s cycles, which remained consistent with the Zumaia record and Site 1209. Furthermore, our result for the number of short eccentricity cycles between MC27r and the LDE ($N = 13$) is consistent with Westerhold et al. (2008) and H15 but differs from D14, who counted cycles 31-32 (from the K/T boundary upwards) as a single cycle (hence their $N = 12$), which leads to age offsets across the interval between our results and D14's tuning (see Table B.2).

Note that Window 4 is by far the largest window introduced here (apart from Window 1, see Zeebe and Lourens, 2019) and hence the match with an astronomical solution across Window 4 in terms of root mean square deviation (RMSD, see Table 4) should be given more weight than the RMSD for other windows. Another important criterion for solution selection is the existence of a very long eccentricity node around 61 Ma, which is based on a robust feature of the geologic records, apparent at different sites and in different proxies (see Section 4.1).

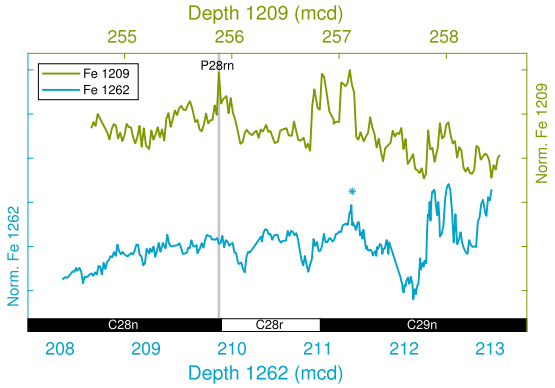

Fig. B.1. Correlation between normalized Fe records at Sites 1209 (green) and 1262 (blue) around P28rn. The Fe peak at 211.4 mcd at Site 1262 (star) could be interpreted to suggest a different correlation, see text.

B.2. Window 5: MC27r to P28rn

In the following, P28rn denotes a peak in the Fe record at 255.9 m at Site 1209 (see Figs. 4 and B.1), close to the C28r/C28n chron boundary. Efforts to obtain a filtered Fe record at Site 1262 for the interval between MC27r and P28rn (as well as between P28rn and the K/T boundary) consistent with the Zumaia record and Site 1209 were unsuccessful. The 1262 filter records yielded insufficient numbers of short eccentricity cycles compared to Zumaia and Site 1209. Attempts to correct for this shortcoming by stretching the record resulted in heavy distortions of e_s amplitudes. Thus, we employed the Fe record at Site 1209 (see Table 3) for Windows 5 and 6.

A Gaussian filter in depth domain centered at 3.45 cycles m^{-1} (bandwidth ±20%) yielded initially $13 \times e_s$ maxima across Window 5 (the count includes the maxima associated with MC27r and P28rn). However, it has been pointed out that the top of this interval is part of a condensed section at Site 1209 (Dinarès-Turell et al., 2014; Westerhold et al., 2008). Visual inspection of the interval would allow for one additional cycle at ~252.8 m, which would also shift MC27r one e_s cycle closer (younger) to the corresponding 405-kyr eccentricity maximum in astronomical solutions, more in line with a stronger expression of MC27r in the sedimentary records. Hence, we stretched the top 1 m of this section, yielding $14 \times e_s$ maxima across Window 5. While of minor importance, we note that $n = 14$ e_s maxima from (and including) MC27r to P28rn is consistent with the cycle count in D14, whereas H15 arrived at $n = 13$.

B.2.1. Correlation between Sites 1262 and 1209 around P28rn

It is noteworthy to comment on the correlation between Sites 1262 and 1209 around P28rn. At Site 1209, P28rn is characterized by a strong Fe peak at ~255.9 mcd (Fig. B.1). Visually, the immediate conclusion would seem that the corresponding Fe peak at Site 1262 (similar shape) is located at 211.4 mcd (Fig. B.1, star). Indeed, this interpretation was favored by Westerhold et al. (2008) (see their Fig. 4, e_s cycle 12 counted from the K/T boundary upwards). However, comparison to Zumaia and magnetostratigraphy suggests a different correlation. Site 1209 lacks a reliable magnetostratigraphy but not Zumaia, where P28rn appears to be located at the chron boundary of C28r and C28n [H15; D14]. Transfer of the cycle counting from Zumaia to Site 1209 then suggests that P28rn at Site 1209 indeed corresponds to the peak at

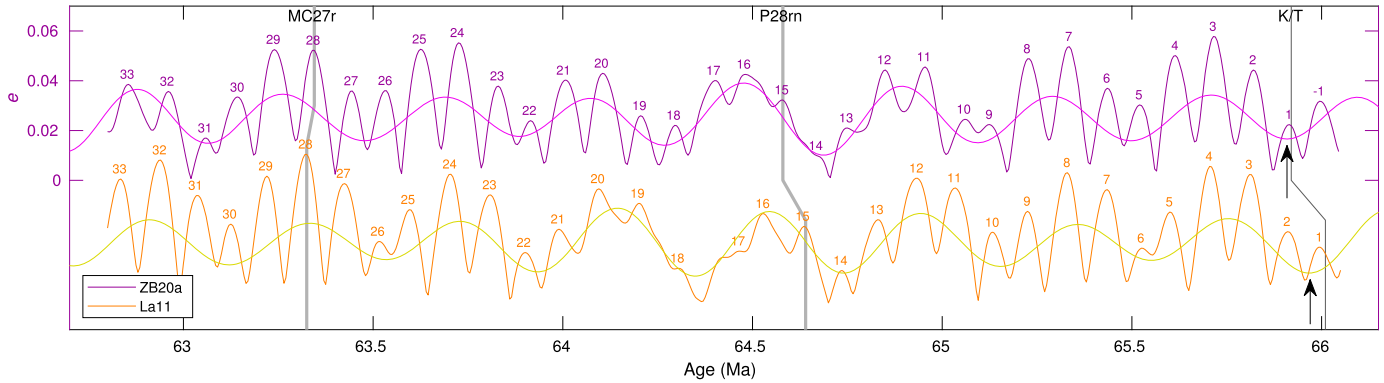

Fig. B.2. Examples of Earth's orbital eccentricity (e) from astronomical solutions relative to early Paleocene events. The solution La11 is plotted with an arbitrary negative offset. MC27r = Middle Chron 27r event, P28rn = Peak near C28r/C28n boundary (Site 1209), K/T = K/T boundary (informal use, see ICS, 2005). Arrows mark the minima in the solutions' long eccentricity (405 kyr) cycle close to the K/T boundary. Numbers label the maxima in the solutions' short eccentricity (~100 kyr) cycle counted from the K/T boundary upwards.

Table B.1
Age of first (oldest) Paleocene long-eccentricity (~405 kyr) minimum for various solutions (see Fig. B.2).

	ZB						La				
	17a	18a	20a	20b	20c	20d	10a	10b	10c	10d	11
$t_{e_l(min_1)}$ [a]	65.96	65.90	65.91	65.91	65.91	65.91	65.92	65.93	65.93	65.98	65.97
Δt_{66} [b]	40	100	90	90	90	90	80	70	70	20	30

[a] (Ma).
[b] (kyr). $\Delta t_{66} = 66$ Ma $- t_{e_l(min_1)}$. Rounded to nearest 10 kyr.

255.9 mcd. At Site 1262 magnetostratigraphy is available, which suggests, however, that the C28r/C28n boundary at Site 1262 is located at ~209.8 mcd [D14], and not at ~211.4 mcd (see Fig. B.1).

This result may appear visually counterintuitive but is inevitable if the magnetostratigraphies at Zumaia and Site 1262, and the cycle counting at Zumaia are accurate. Importantly though, the correlation between Sites 1262 and 1209 around P28rn only affects the tie points for Site 1262 for this section. It does not affect our final Paleocene age model, which is based on Site 1209 all the way from MC27r to the K/T boundary (see Fig. 4; the correlation between Sites 1262 and 1209 around MC27r seems uncontroversial).

B.3. Window 6: P28rn to K/T boundary

Based on the correlation between the Zumaia record and Site 1209, both H15 and D14 suggest P28rn to be associated with the maximum of e_s cycle 15, counted from the K/T boundary upwards and tuned to the orbital solution La11 (Laskar et al., 2011a) (used in H15 and preferred by D14, see Fig. B.2). The cycle counting and numbering requires some explanation though. The K/T boundary appears to occur close to a long eccentricity (405 kyr) ***minimum*** (Fig. B.2, arrows). The ***maximum*** of the corresponding short eccentricity cycle is assigned e_s cycle Nº 1 here, where corresponding means following a larger e_s maximum associated with the final, youngest Cretaceous 405-kyr cycle. Importantly, because the g_2–g_5 cycle (~405 kyr) differs slightly between astronomical solutions, the age model and, e.g., the inferred K/T boundary age therefore depend on the astronomical solution used for tuning and correlates with the solutions' ages of the first (oldest) Paleocene long-eccentricity minimum (Table B.1).

The above cycle counting and assignment is consistent with H15 (see age/eccentricity axis tuned to La11 in their Fig. 3). The counting is also consistent with D14, but their number assignment is different (see their Fig. 5). D14's number assignment follows the original eccentricity maxima numbering by Westerhold et al. (2008) to which D14 added letter subscripts for newly identified cycles. For example, between P28rn and the K/T boundary, D14 added cycle 12b. Thus, while D14 labeled P28rn cycle Nº 14 (see their Fig. 5), it is actually cycle 15 (counted from the K/T boundary upwards and tuned to La11). In addition, as noted above, the age model and hence cycle numbers can differ between astronomical solutions. For instance, P28rn is associated with the maximum of e_s cycle 15 in the solutions ZB20a and La11 (Fig. B.2) but with cycle 14 in ZB18a and La10b, for example (solutions ZB18a and La10b not shown, but see Table 4). The amplitude of the solution's e_s maximum at P28rn then becomes an additional selection criterion for a proper solution. Given that P28rn is associated with a strong peak in the sedimentary record (e.g., in Fe at Site 1209), it is unlikely that the eccentricity forcing was associated with a weak e_s maximum, for instance, occurring close to a long eccentricity minimum. Instead, it is more likely that P28rn was associated with a strong e_s maximum.

The above criterion rules out a number of astronomical solutions (see also Section 2). If the K/T boundary coincides with an e_l minimum, then the subsequent large e_s maxima may occur at short cycles 4, 8, 12, 16, ... (La11), as 4 short cycles approximately equal one long cycle, i.e., n for large e_s maxima is given by $n_{i+1} = n_i + 4$ (see Fig. B.2). However, the P28rn criterion requires that exactly cycle Nº 15 (e.g., La11) be a large e_s maximum, although 15 is not part of the above sequence. In many solutions these preceding cycles (preceding a large e_s maximum that *is* part of the sequence) have only intermediate or weak amplitude. Also, while the preceding cycles may be strong across other 405-kyr cycles of a solution, the requirement to occur exactly at P28rn poses an important restriction.

Alternatively, if P28rn was actually associated with the maximum of e_s cycle Nº 16, many more solutions would fit this criterion. However, it would effectively require that chron C28r spans two e_s maxima, not one (adding another e_s cycle below Nº 13 is difficult due to the required match with the 405-kyr cycle). While this appears not impossible for the deep-sea records at Sites 1262 and 1209 (see Fig. B.1), it would be inconsistent with the Zumaia record, the latter of which we assume here to be accurate for the time being. Finally, note that due to the aftermath of the K/T

Table B.2
Paleocene tie points[a], events, and astronomical ages.

Nº	Event[b]	1262 (mcd)[c]	†	1209 (mcd)[c]	†	Age (Ma) ZBx 18a	20a	20b	20c	20d
	K/T	216.7		261.6		65.94	65.92	65.92	65.95	65.95
1		215.2	?	260.4		65.73	65.72	65.72	65.74	65.74
2		213.3		258.8		65.33	65.33	65.34	65.32	65.34
3		211.4		257.1		64.93	64.96	64.96	64.92	64.91
4	P28rn	209.7	?	255.9		64.65	64.58	64.58	64.64	64.62
5			?	254.5		64.10	64.11	64.11	64.14	64.13
6		205.7	?	253.4		63.72	63.73	63.72	63.72	63.76
7	MC27r	204.1		252.5		63.34	63.34	63.34	63.33	63.35
8		200.9	?,c	251.3	?	62.85	62.85	62.85	62.84	62.83
9		198.4		250.1		62.42	62.42	62.42	62.46	62.43
10	LDE	195.3		248.1		62.03	62.03	62.03	62.02	62.04
11		192.1		246.0	?	61.64	61.65	61.66	61.64	61.66
12		188.7		243.2		61.24	61.25	61.26	61.24	61.22
13		185.4			?,c	60.91	60.91	60.93	60.95	60.92
14	P26r	181.6		240.9		60.42	60.42	60.44	60.42	60.44
15		178.5		238.8		60.04	60.04	60.05	60.04	60.05
16		175.4		236.9	?	59.66	59.66	59.66	59.66	59.61
17	ELPE	173.7		235.1		59.23	59.24	59.23	59.23	59.23
18		171.5		234.2	?	58.83	58.83	58.84	58.83	58.85
19		168.7		231.8	?	58.46	58.45	58.46	58.45	58.47
20	PCIM	165.9		230.1	?	58.06	58.05	58.07	58.05	58.05
21		159.8		226.6	?	57.65	57.65	57.64	57.64	57.64
22	B2	155.6		224.0		57.24	57.24	57.24	57.24	57.25
23	C1	150.6		221.4		56.85	56.85	56.85	56.85	56.85
24	D1	146.0		220.0	?,c	56.47	56.47	56.47	56.47	56.47
25	P/E	140.1		218.0		56.01	56.01	56.01	56.01	56.01

[a] Based on Fe records from Ocean Drilling Program Sites 1262 and 1209.
[b] K/T = K/T boundary, P28rn = Peak near C28r/C28n boundary (Site 1209), MC27r = Middle Chron 27r event, LDE = Latest Danian Event, P26r = Peak Chron 26r (middle), ELPE = Early Late Paleocene Event, PCIM = Paleocene Carbon Isotope Maximum, B2, C1, D1 = Eocene thermal events (see e.g., Lauretano et al., 2016), P/E = Paleocene/Eocene boundary.
[c] mcd = meters composite depth.
† Notes: ? = uncertain, c = condensed section.

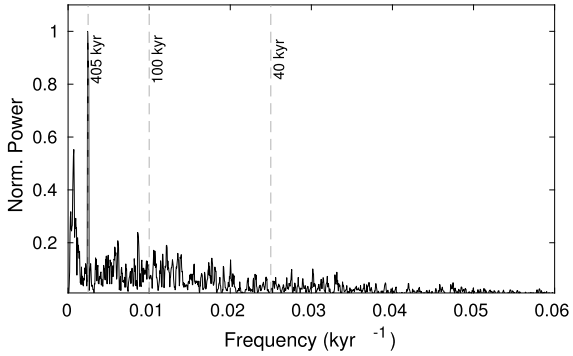

Fig. C.1. Multitaper method (MTM) spectral analysis results (this study) of gamma-ray (GR) logs from the BS1 borehole (Xu et al., 2019) after tuning to the 405-kyr cycle. The MTM analysis used $K = 3$ tapers with $K = 2q - 1$, where $q = 2$ is the time-bandwidth product. Note little to no power in the obliquity band around 40 kyr.

impact and generally low/variable sedimentation rates, we cannot exclude filter distortions throughout Window 6. Hence the match with an astronomical solution across Window 6 in terms of RMSD (see Table 4) is given less weight than the RMSD for other windows.

Appendix C. Potential obliquity records

As explained in Section 6.1, suitable obliquity records across the Paleocene would be desirable to also examine $s_4 - s_3$ in the geologic record, i.e., via amplitude modulation (AM) of obliquity. Here we briefly discuss three potential candidates for such records from China (Liu et al., 2018, 2019; Xu et al., 2019). Xu et al. (2019) analyzed gamma-ray (GR) logs from the B270 and BS1 boreholes in the Nanxiang Basin, of which only BS1 covers the Paleocene though. After following their tuning to the 405-kyr cycle, our GR-MTM spectrum at BS1 shows some power in the 100-kyr band but little to no power in the obliquity band (around 40 kyr, Fig. C.1). For the current purpose of constraining astronomical solutions using geologic records, a strong and robust signal at or near the astronomical frequency in question is required. This is not the case for the BS1-GR record at or near the 40-kyr band (Fig. C.1). A similar argument can be made for a GR record from the Bohai Bay Basin (see Fig. 8C in Liu et al., 2018). Thus, these records unlikely provide any rigorous constraints on $s_4 - s_3$ and allow unambiguous selection of suitable astronomical solutions.

Liu et al. (2019) (L19) examined GR profiles from the WP-1 borehole in the East China Sea Shelf Basin and reported a prominent ~1.2-Myr periodicity, owing to the AM of obliquity. Starting with the GR data in depth domain, we attempted to repeat their analysis and obtained a normalized GR record in the time domain very similar to the published one (compare Fig. C.2a and d). However, L19's and our 41-kyr filters of the GR records and the corresponding Hilbert transforms show differences. For example, L19's 41-kyr filter has a large amplitude around 6.5 Myr (floating chronology), whereas our filter does not (compare Fig. C.2b and e). Furthermore, the MTM spectra of the Hilbert transform show little resemblance (compare Fig. C.2g and h). Whereas L19's Hilbert spectrum shows an absolute maximum at ~1.2 Myr (see also filter Fig. C.2c), our Hilbert spectrum does not. Rather, we find significant power around 6 Myr, ~2 Myr and ~630 kyr (for 630 kyr filter, see Fig. C.2f). As a result, we were unable to reproduce L19's results of a prominent ~1.2-Myr periodicity in the WP-1 GR record

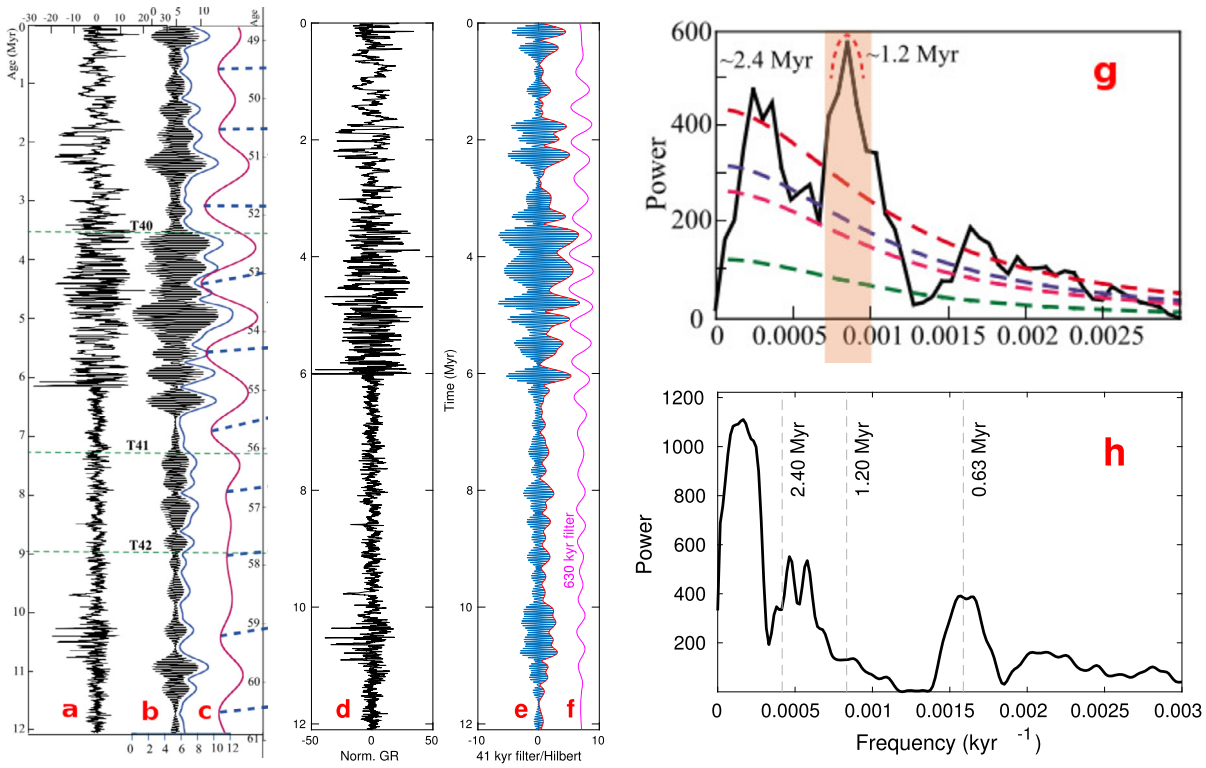

Fig. C.2. Comparison of analyses of gamma-ray (GR) profiles from the WP-1 borehole by Liu et al. (2019) and this study. (a) Detrended and tuned GR record, (b) Hilbert transform, and (c) 1.2 Myr filter (figures from Liu et al. (2019)). (d) Detrended and tuned GR record, (e) Hilbert transform, and (f) 630 kyr filter (this study). Note large 41-kyr filter amplitude around 6.5 Myr (floating chronology, Liu et al. (2019), panel (b)), which is absent in our results (e). (g) MTM spectrum of the Hilbert transform from Liu et al. (2019), showing little resemblance to our MTM Hilbert spectrum (h).

(indispensable to constrain $s_4 - s_3$), the cause of which is unclear at this point.

References

Barnet, J.S.K., Littler, K., Westerhold, T., Kroon, D., Leng, M.J., Bailey, I., Röhl, U., Zachos, J.C., 2019. A high-fidelity benthic stable isotope record of late Cretaceous–early Eocene climate change and carbon-cycling. Paleoceanogr. Paleoclimatol. 34 (4), 672–691.

Batenburg, S.J., Sprovieri, M., Gale, A.S., Hilgen, F.J., Hüsing, S., Laskar, J., Liebrand, D., Lirer, F., Orue-Etxebarria, X., Pelosi, N., Smit, J., 2012. Cyclostratigraphy and astronomical tuning of the Late Maastrichtian at Zumaia (Basque country, Northern Spain). Earth Planet. Sci. Lett. 359, 264–278. https://doi.org/10.1016/j.epsl.2012.09.054.

Clyde, W.C., Ramezani, J., Johnson, K.R., Bowring, S.A., Jones, M.M., 2016. Direct high-precision U-Pb geochronology of the end-Cretaceous extinction and calibration of Paleocene astronomical timescales. Earth Planet. Sci. Lett. 452, 272–280. https://doi.org/10.1016/j.epsl.2016.07.041.

Cramwinckel, M.J., Huber, M., Kocken, I.J., Agnini, C., Bijl, P.K., Bohaty, S.M., Frieling, J., Goldner, A., Hilgen, F.J., Kip, E.L., Peterse, F., van der Ploeg, R., Röhl, U., Schouten, S., Sluijs, A., 2018. Synchronous tropical and polar temperature evolution in the Eocene. Nature 559 (7714), 382–386. https://doi.org/10.1038/s41586-018-0272-2.

Dinarès-Turell, J., Westerhold, T., Pujalte, V., Röhl, U., Kroon, D., 2014. Astronomical calibration of the Danian stage (Early Paleocene) revisited: settling chronologies of sedimentary records across the Atlantic and Pacific Oceans. Earth Planet. Sci. Lett. 405, 119–131. https://doi.org/10.1016/j.epsl.2014.08.027.

Einstein, A., 1916. Die Grundlage der allgemeinen Relativitätstheorie. Ann. Phys. VI 49 (7), 769–822. https://doi.org/10.1002/andp.19163540702.

Fienga, A., Laskar, J., Morley, T., Manche, H., Kuchynka, P., Le Poncin-Lafitte, C., Budnik, F., Gastineau, M., Somenzi, L., 2009. INPOP08, a 4-D planetary ephemeris: from asteroid and time-scale computations to ESA Mars Express and Venus Express contributions. Astron. Astrophys. 507, 1675–1686. https://doi.org/10.1051/0004-6361/200911755.

Fienga, A., Manche, H., Laskar, J., Gastineau, M., Verma, A., 2014. Inpop new release: Inpop13b. arXiv:1405.0484.

Folkner, W.M., Williams, J.G., Boggs, D.H., Park, R.S., Kuchynka, P., 2014. The planetary and lunar ephemerides DE430 and DE431. Interplanetary Network Progress Report, 196.

Gilabert, V., Batenburg, S.J., Arenillas, I., Arz, J.A., 2022. Contribution of orbital forcing and Deccan volcanism to global climatic and biotic changes across the Cretaceous-Paleogene boundary at Zumaia, Spain. Geology 50 (1), 21–25. https://doi.org/10.1130/G49214.1.

Gradstein, F.M., Ogg, J.G., Hilgen, F.J., 2012. On the geologic time scale. Newsl. Stratigr. 45 (2), 171–188. https://doi.org/10.1127/0078-0421/2012/0020.

Hilgen, F.J., Kuiper, K.F., Lourens, L.J., 2010. Evaluation of the astronomical time scale for the Paleocene and earliest Eocene. Earth Planet. Sci. Lett. 300, 139–151. https://doi.org/10.1016/j.epsl.2010.09.044.

Hilgen, F.J., Abels, H.A., Kuiper, K.F., Lourens, L.J., Wolthers, M., 2015. Towards a stable astronomical time scale for the Paleocene: aligning Shatsky Rise with the Zumaia–Walvis Ridge ODP Site 1262 composite. Newsl. Stratigr. 48 (1), 91–110.

Hinnov, L.A., 2000. New perspectives on orbitally forced stratigraphy. Annu. Rev. Earth Planet. Sci. 28, 419–475. https://doi.org/10.1146/annurev.earth.28.1.419.

Holmes, A., 1965. Principles of Physical Geology. Nelson Ltd., UK, p. 1288.

ICS, 2005. Definition and Rank of Quaternary, International Commission on Stratigraphy. https://stratigraphy.org/files/Q1.pdf.

Kuiper, K.F., Deino, A., Hilgen, F.J., Krijgsman, W., Renne, P.R., Wijbrans, J.R., 2008. Synchronizing rock clocks of Earth history. Science 320 (5875), 500–504. https://doi.org/10.1126/science.1154339.

Lantink, M.L., Davies, J.H.F.L., Mason, P.R.D., Schaltegger, U., Hilgen, F.J., 2019. Climate control on banded iron formations linked to orbital eccentricity. Nat. Geosci. 12 (5), 369–374. https://doi.org/10.1038/s41561-019-0332-8.

Laskar, J., 1989. A numerical experiment on the chaotic behaviour of the solar system. Nature 338, 237–238. https://doi.org/10.1038/338237a0.

Laskar, J., 1990. The chaotic motion of the solar system - a numerical estimate of the size of the chaotic zones. Icarus 88, 266–291. https://doi.org/10.1016/0019-1035(90)90084-M.

Laskar, J., Robutel, P., Joutel, F., Gastineau, M., Correia, A.C.M., Levrard, B., 2004. A long-term numerical solution for the insolation quantities of the Earth. Astron. Astrophys. 428, 261–285. https://doi.org/10.1051/0004-6361:20041335.

Laskar, J., Fienga, A., Gastineau, M., Manche, H., 2011a. La2010: a new orbital solution for the long-term motion of the Earth. Astron. Astrophys. 532, A89. https://doi.org/10.1051/0004-6361/201116836.

Laskar, J., Gastineau, M., Delisle, J.-B., Farrés, A., Fienga, A., 2011b. Strong chaos induced by close encounters with Ceres and Vesta. Astron. Astrophys. 532, L4. https://doi.org/10.1051/0004-6361/201117504.

Lauretano, V., Hilgen, F., Zachos, J., Lourens, L., 2016. Astronomically tuned age model for the early Eocene carbon isotope events: a new high-resolution $\delta^{13}C$ benthic record of ODP Site 1263 between ~49 and ~54 Ma. Newsl. Stratigr. 49, 383–400. https://doi.org/10.1127/nos/2016/0077.

Lauretano, V., Zachos, J.C., Lourens, L.J., 2018. Orbitally paced carbon and deep-sea temperature changes at the peak of the Early Eocene Climatic Optimum. Paleoceanogr. Paleoclimatol. 33 (10), 1050–1065.

Li, M., Kump, L.R., Hinnov, L.A., Mann, M.E., 2018. Tracking variable sedimentation rates and astronomical forcing in Phanerozoic paleoclimate proxy series with evolutionary correlation coefficients and hypothesis testing. Earth Planet. Sci. Lett. 501, 165–179. https://doi.org/10.1016/j.epsl.2018.08.041.

Liebrand, D., Beddow, H.M., Lourens, L.J., Pälike, H., Raffi, I., Bohaty, S.M., Hilgen, F.J., Saes, M.J.M., Wilson, P.A., van Dijk, A.E., 2016. Cyclostratigraphy and eccentricity tuning of the early Oligocene through early Miocene (30.1-17.1 Ma): cibicides mundulus stable oxygen and carbon isotope records from Walvis Ridge Site 1264. Earth Planet. Sci. Lett. 450, 392–405. https://doi.org/10.1016/j.epsl.2016.06.007.

Liu, Y., Huang, C., Ogg, J.G., Algeo, T.J., Kemp, D.B., Shen, W., 2019. Oscillations of global sea-level elevation during the Paleogene correspond to 1.2-Myr amplitude modulation of orbital obliquity cycles. Earth Planet. Sci. Lett. 522, 65–78. https://doi.org/10.1016/j.epsl.2019.06.023.

Liu, Z., Huang, C., Algeo, T.J., Liu, H., Hao, Y., Du, X., Lu, Y., Chen, P., Guo, L., Peng, L., 2018. High-resolution astrochronological record for the Paleocene-Oligocene (66-23 Ma) from the rapidly subsiding Bohai Bay Basin, northeastern China. Palaeogeogr. Palaeoclimatol. Palaeoecol. 510, 78–92. https://doi.org/10.1016/j.palaeo.2017.10.030.

Lourens, L.J., Sluijs, A., Kroon, D., Zachos, J.C., Thomas, E., Röhl, U., Bowles, J., Raffi, I., 2005. Astronomical pacing of late Palaeocene to early Eocene global warming events. Nature 435, 1083–1087. https://doi.org/10.1038/nature03814.

Ma, C., Meyers, S.R., Sageman, B.B., 2017. Theory of chaotic orbital variations confirmed by Cretaceous geological evidence. Nature 542, 468–470. https://doi.org/10.1038/nature21402.

Meyers, S.R., 2014. Astrochron: an R package for astrochronology. cran.r-project.org/web/packages/astrochron/index.html.

Meyers, S.R., 2015. The evaluation of eccentricity-related amplitude modulation and bundling in paleoclimate data: an inverse approach for astrochronologic testing and time scale optimization. Paleoceanography 30, 1625–1640.

Nobili, A.M., Milani, A., Carpino, M., 1989. Fundamental frequencies and small divisors in the orbits of the outer planets. Astron. Astrophys. 210, 313–336.

Pälike, H., Laskar, J., Shackleton, N.J., 2004. Geologic constraints on the chaotic diffusion of the solar system. Geology 32, 929. https://doi.org/10.1130/G20750.1.

Park, R.S., Folkner, W.M., Konopliv, A.S., Williams, J.G., Smith, D.E., Zuber, M.T., 2017. Precession of Mercury's perihelion from ranging to the MESSENGER spacecraft. Astron. J. 153, 121. https://doi.org/10.3847/1538-3881/aa5be2.

Park, R.S., Folkner, W.M., Williams, J.G., Boggs, D.H., 2021. The JPL planetary and lunar ephemerides DE440 and DE441. Astron. J. 161 (3), 105. https://doi.org/10.3847/1538-3881/abd414.

Pijpers, F.P., 1998. Helioseismic determination of the solar gravitational quadrupole moment. Mon. Not. R. Astron. Soc. 297, L76–L80. https://doi.org/10.1046/j.1365-8711.1998.01801.x.

Quinn, T.R., Tremaine, S., Duncan, M., 1991. A three million year integration of the Earth's orbit. Astron. J. 101, 2287–2305. https://doi.org/10.1086/115850.

Rauch, K.P., Hamilton, D.P., 2002. The HNBody package for symplectic integration of nearly-Keplerian systems. In: AAS/Division of Dynamical Astronomy Meeting #33. Bull. Am. Astron. Soc. 34, 938.

Renne, P.R., Balco, G., Ludwig, K.R., Mundil, R., Min, K., 2011. Response to the comment by W.H. Schwarz et al. on "Joint determination of ^{40}K decay constants and ^{40}Ar*/^{40}K for the Fish Canyon sanidine standard, and improved accuracy for ^{40}Ar/^{39}Ar geochronology" by P.R. Renne et al. (2010). Geochim. Cosmochim. Acta 75 (17), 5097–5100. https://doi.org/10.1016/j.gca.2011.06.021.

Renne, P.R., Deino, A.L., Hilgen, F.J., Kuiper, K.F., Mark, D.F., Mitchell, W.S., Morgan, L.E., Mundil, R., Smit, J., 2013. Time scales of critical events around the Cretaceous-Paleogene boundary. Science 339 (6120), 684–687. https://doi.org/10.1126/science.1230492.

Schaen, A.J., Jicha, B.R., Hodges, K.V., Vermeesch, P., Stelten, M.E., Mercer, C.M., Phillips, D., Rivera, T.A., Jourdan, F., Matchan, E.L., Hemming, S.R., Morgan, L.E., Kelley, S.P., Cassata, W.S., Heizler, M.T., Vasconcelos, P.M., Benowitz, J.A., Koppers, A.A., Mark, D.F., Niespolo, E.M., Sprain, C.J., Hames, W.E., Kuiper, K.F., Turrin, B.D., Renne, P.R., Ross, J., Nomade, S., Guillou, H., Webb, L.E., Cohen, B.A., Calvert, A.T., Joyce, N., Ganerod, M., Wijbrans, J., Ishizuka, O., He, H., Ramirez, A., Pfaender, J.A., Lopez-Martinez, M., Qiu, H., Singer, B.S., 2020. Interpreting and reporting ^{40}Ar/^{39}Ar geochronologic data. Geol. Soc. Am. Bull. https://doi.org/10.1130/B35560.1.

Sprain, C.J., Renne, P.R., Clemens, W.A., Wilson, G.P., 2018. Calibration of chron C29r: new high-precision geochronologic and paleomagnetic constraints from the Hell Creek region, Montana. Geol. Soc. Am. Bull. 130 (9–10), 1615–1644. https://doi.org/10.1130/B31890.1.

Sussman, G.J., Wisdom, J., 1988. Numerical evidence that the motion of Pluto is chaotic. Science 241 (4864), 433–437. https://doi.org/10.1126/science.241.4864.433.

Sussman, G.J., Wisdom, J., 1992. Chaotic evolution of the solar system. Science 257, 56–62. https://doi.org/10.1126/science.257.5066.56.

Viswanathan, V., Fienga, A., Gastineau, M., Laskar, J., 2017. INPOP17a planetary ephemerides. IMCCE, Scientific Notes. www.imcce.fr/recherche/equipes/asd/inpop/download17a.

Westerhold, T., Röhl, U., Raffi, I., Fornaciari, E., Monechi, S., Reale, V., Bowles, J., Evans, H.F., 2008. Astronomical calibration of the Paleocene time. Palaeogeogr. Palaeoclimatol. Palaeoecol. 257 (4), 377–403.

Westerhold, T., Röhl, U., Frederichs, T., Agnini, C., Raffi, I., Zachos, J.C., Wilkens, R.H., 2017. Astronomical calibration of the Ypresian timescale: implications for seafloor spreading rates and the chaotic behavior of the solar system? Clim. Past 13 (9), 1129–1152. https://doi.org/10.5194/cp-13-1129-2017.

Xu, K., Chen, H., Huang, C., Ogg, J.G., Zhu, J., Lin, S., Yang, D., Zhao, P., Kong, L., 2019. Astronomical time scale of the Paleogene lacustrine paleoclimate record from the Nanxiang Basin, central China. Palaeogeogr. Palaeoclimatol. Palaeoecol. 109, 253. https://doi.org/10.1016/j.palaeo.2019.109253.

Zachos, J.C., Röhl, U., Schellenberg, S.A., Sluijs, A., Hodell, D.A., Kelly, D.C., Thomas, E., Nicolo, M., Raffi, I., Lourens, L.J., McCarren, H., Kroon, D., 2005. Rapid acidification of the ocean during the Paleocene-Eocene Thermal Maximum. Science 308, 1611–1615.

Zeebe, R.E., 2015a. Dynamic stability of the Solar System: statistically inconclusive results from ensemble integrations. Astrophys. J. 798, 8. https://doi.org/10.1088/0004-637X/798/1/8.

Zeebe, R.E., 2015b. Highly stable evolution of Earth's future orbit despite chaotic behavior of the Solar System. Astrophys. J. 811, 9. https://doi.org/10.1088/0004-637X/811/1/9.

Zeebe, R.E., 2017. Numerical solutions for the orbital motion of the Solar System over the Past 100 Myr: limits and new results. Astron. J. 154, 193. https://doi.org/10.3847/1538-3881/aa8cce.

Zeebe, R.E., Lourens, L.J., 2019. Solar system chaos and the Paleocene-Eocene boundary age constrained by geology and astronomy. Science 365, 926–929.

Zeebe, R.E., Lourens, L.J., 2022. A deep-time dating tool for paleo-applications utilizing obliquity and precession cycles: the role of dynamical ellipticity and tidal dissipation. Paleoceanogr. Paleoclimatol.

Zeebe, R.E., Ridgwell, A., Zachos, J.Z., 2016. Anthropogenic carbon release rate unprecedented during past 66 million years. Nat. Geosci. 9, 325–329. https://doi.org/10.1038/NGEO2681.